

Adiabatic and non-adiabatic phonon dispersion in a Wannier function approach

Matteo Calandra¹, Gianni Profeta², and Francesco Mauri¹

¹*CNRS and Institut de Minéralogie et de Physique des Milieux condensés,
case 115, 4 place Jussieu, 75252, Paris cedex 05, France and*

²*Consiglio Nazionale delle Ricerche - Superconducting and Innovative Devices (CNR-SPIN), 67100 L'Aquila, Italy*

(Dated: November 3, 2018)

We develop a first-principles scheme to calculate adiabatic and non-adiabatic phonon frequencies in the full Brillouin zone. The method relies on the variational properties of a force-constants functional with respect to the first-order perturbation of the electronic charge density and on the localization of the deformation potential in the Wannier function basis. This allows for calculation of phonon dispersion curves free from convergence issues related to Brillouin zone sampling. In addition our approach justifies the use of the static screened potential in the calculation of the phonon linewidth due to decay in electron-hole pairs. We apply the method to the calculation of the phonon dispersion and electron-phonon coupling in MgB₂ and CaC₆. In both compounds we demonstrate the occurrence of several Kohn anomalies, absent in previous calculations, that are manifest only after careful electron and phonon momentum integration. In MgB₂, the presence of Kohn anomalies on the E_{2g} branches improves the agreement with measured phonon spectra and affects the position of the main peak in the Eliashberg function. In CaC₆ we show that the non-adiabatic effects on in-plane carbon vibrations are not localized at zone center but are sizable throughout the full Brillouin zone. Our method opens new perspectives in large-scale first-principles calculations of dynamical properties and electron-phonon interaction.

PACS numbers: 63.20.dk, 71.15.-m, 63.20.kd

I. INTRODUCTION

Electron-phonon (EP) interaction is responsible of many important phenomena in solids. As an example, the temperature behavior of the electron relaxation time in metals is to a great extent due to the scattering between carriers and atomic vibrations¹ such that finite temperature transport is largely ruled by the EP interaction. Similarly, the high temperature heat capacity in metals is enhanced by the increased electronic mass due to the interaction with lattice vibrations². In metals, at low temperatures, EP coupling can generate a superconducting state in which electrons move with no electrical resistance³. It also can increase the effective mass of the carriers so much that the system is driven from a metallic to an insulating state, as it happens in case of polaronic or Peierls instabilities⁴. Finally, the electron-phonon scattering is often the largest source of phonon damping in phonon-mediated superconductors⁵.

First-principles theoretical determination of the electron-phonon coupling strength in solids requires the calculation of the electronic structure, the vibrational properties, and the electron-phonon coupling matrix elements. In state-of-the-art electronic structure calculations these quantities are obtained using the adiabatic Born-Oppenheimer approximation⁶ and density-functional theory (DFT) in the linear-response approach⁷⁻⁹.

More specifically, within the Born-Oppenheimer approximation, the determination of phonon frequencies, that are related to the real part of the phonon self-energy, requires the calculation, *in a self-consistent manner*, of the variation of the Kohn-Sham potential V_{SCF} with respect to a *static* ionic displacement \mathbf{u} ⁷, namely

$\frac{\delta V_{\text{SCF}}(\mathbf{r})}{\delta \mathbf{u}}$. As the displacement of the ions is static, the obtained $\frac{\delta V_{\text{SCF}}(\mathbf{r})}{\delta \mathbf{u}}$ is real. Conversely, the phonon linewidth, related to the imaginary part of the phonon self-energy, is obtained in a *non self-consistent* procedure using the electron charge density and the previously determined $\frac{\delta V_{\text{SCF}}(\mathbf{r})}{\delta \mathbf{u}}$. The advantage of using a non self-consistent procedure to study phonon linewidth is mainly related to the less expensive computational load with respect to a self-consistent one. In addition, as recently demonstrated, interpolation schemes^{10,11} of the electron-phonon matrix elements can be used to calculate the imaginary part of the phonon self-energy on ultra-dense k-point grid.

It is however unclear to what extent this procedure of calculating self-consistently the real part of the phonon self-energy and non self-consistently the imaginary part is actually correct. Indeed, the proper way of treating phonons should be to consider a monochromatic time-dependent displacement (at the phonon frequency ω) and perform a time-dependent self-consistent linear-response scheme. The resulting variation of the self-consistent potential $\frac{\delta V_{\text{SCF}}(\mathbf{r}, \omega)}{\delta \mathbf{u}}$ would then be a complex quantity. The real part of the resulting phonon self-energy would then determine the phonon frequencies while its imaginary part would lead to the phonon linewidth. In this way, non-adiabatic (in the sense of Ref. 12) *dynamical* phonon frequencies could be accessed. Although feasible in principle this procedure would require a full rewriting of the linear response code including time dependence and it would also be more expensive than a standard static linear-response calculation. Moreover, in the presence of Kohn anomalies and long-range force-constants, where extremely accurate k-point sampling of the Fermi

surface is needed to converge the phonon self-energy, the calculation would be unfeasible.

Thus, it would be desirable to have a non-self-consistent linear-response formulation to obtain both the real and imaginary phonon self-energy, both within the adiabatic/static and non-adiabatic/dynamic approximation.

In this work we develop a scheme to calculate non self-consistently both the real and the imaginary part of the phonon self-energy by using a functional that is variational with respect to the variation of the self-consistent charge density. Our method opens the way to calculate adiabatic/static and non-adiabatic/dynamic phonon frequencies using an ultra-dense sampling of the electron and phonon wave-vector in a non self-consistent way, starting from the static self-consistent variation of the time independent Kohn-Sham potential ($\frac{\delta V_{\text{SCF}}(\mathbf{r})}{\delta \mathbf{u}}$), obtained with a coarse sampling. In this way, the main computational load related to phonon frequencies calculation is drastically reduced. The efficiency of the method is further enhanced by using the interpolation of the electron-phonon matrix elements¹³ based on Wannier functions¹⁴.

The method is applied to study the dynamical and superconducting properties of MgB₂ and CaC₆, two of the most studied superconducting materials in the last few years. These applications are meaningful and computationally challenging. In fact, although many experimental and theoretical studies appeared, there are still important open issues and debated results.

For example, conflicting results for the calculate MgB₂ electron-phonon coupling (λ) are present in the literature mainly due to difficulties in Brillouin Zone sampling. This, apart its fundamental importance, prevents a full understanding of the normal and superconducting properties of this material.

In the case of CaC₆, very large non-adiabatic effects were predicted¹² and measured¹⁵ at zone-center. It is unclear to what extend non-adiabatic effects are sizable far from Γ -point. In this last case, the adiabatic effects can be relevant for thermodynamic properties resulting from an average of the phonon frequencies over the Brillouin zone.

The paper is organized as follows. In Section II we derive the variational formulation of the force-constant matrix. This will be done starting from the formal definition of force constants in the case of a monochromatic time-dependent ionic displacement (Sec.II A). In Sec. II B we discuss when non-adiabatic/dynamic effects should be expected in the phonon spectra. The linear response equations for the dynamical matrix are introduced (Sec.II C) in the general case and then specialized in the density functional formulation (Sec.II D).

In Section II E, we develop the variational formulation of the force constants in the density functional linear-response theory and outline the computational framework of phonon and electron-phonon coupling (Sec.II F and II G). In Sec. II H we show how our approach justify the use of the static screened potential in the calculation of the phonon linewidth due to decay in electron-hole

pairs. Section III will be devoted to the description of the implementation of the theory using the Wannier interpolation scheme.

In Section IV we reports results on dynamical and superconducting properties of MgB₂ (Sec.IV A) and CaC₆ (Sec.IV B).

Section V summarizes our conclusions.

II. THEORY

A. Time dependent dynamical matrix and phonon damping.

We consider a crystal with N atoms in the unit cell submitted to a time dependent perturbation, in which the position of an atom is identified by the vector

$$\mathbf{R}_I \equiv \mathbf{R}_L + \boldsymbol{\tau}_s + \mathbf{u}_I(t), \quad (1)$$

where \mathbf{R}_L is the position of the L -th unit cell in the Bravais lattice, $\boldsymbol{\tau}_s$ is the equilibrium position of the s -th atom in the unit cell, $\mathbf{u}_I(t)$ indicates the deviation from equilibrium of the nuclear position and $I = \{L, s\}$. The force at time t acting on the J -th nucleus ($J = \{M, r\}$) due to the displacement $\mathbf{u}_I(t')$ of the atom I -th at time t' is labeled $\mathbf{F}_J(t)$. The force constants matrix is defined as:

$$C_{IJ}(\mathbf{R}_L - \mathbf{R}_M; t - t') = -\frac{\delta \mathbf{F}_J(t)}{\delta \mathbf{u}_I(t')} \quad (2)$$

where we used the translational invariance of the crystal and make evident the dependence of C_{IJ} on the lattice vector $\mathbf{R}_L - \mathbf{R}_M$ (to lighten the notation we omit it in the following equations where no confusion may arise). The ω -transform of the force-constants matrix is thus:

$$C_{IJ}(\omega) = \int dt e^{i\omega t} C_{IJ}(t) \quad (3)$$

While the force-constants matrix $C_{IJ}(t)$ is a real quantity, its ω -transform $C_{IJ}(\omega)$ is not real and has both a real and imaginary part. The Fourier transform of the force-constant matrix is

$$C_{sr}(\mathbf{q}, \omega) = \sum_L e^{-i\mathbf{q}\mathbf{R}_L} C_{Ls, Mr}(\omega) \quad (4)$$

where, without loss of generality, we have chosen $\mathbf{R}_M = \mathbf{0}$. The Hermitian and anti-Hermitian combination of the force-constant matrix in momentum space are:

$$D_{sr}(\mathbf{q}, \omega) = \frac{1}{2\sqrt{M_s M_r}} [C_{sr}(\mathbf{q}, \omega) + C_{rs}(\mathbf{q}, \omega)^*] \quad (5)$$

$$A_{sr}(\mathbf{q}, \omega) = \frac{1}{2i\sqrt{M_s M_r}} [C_{sr}(\mathbf{q}, \omega) - C_{rs}(\mathbf{q}, \omega)^*] \quad (6)$$

where M_s is the mass of the s -th atom in the unit cell. These quantities are associated to the real and imaginary

part of the dynamical matrix in coordinate space. If the imaginary part of the dynamical matrix is small with respect to its real part, namely

$$|A_{sr}(\mathbf{q}, \omega)| \ll |D_{sr}(\mathbf{q}, \omega)| \quad (7)$$

then the self-consistent condition

$$\det |D_{sr}(\mathbf{q}, \omega_{\mathbf{q}\nu}) - \omega_{\mathbf{q}\nu}^2| = 0 \quad (8)$$

determines non-adiabatic/dynamic phonon frequencies $\omega_{\mathbf{q}\nu}$ and phonon eigenvectors $\{\mathbf{e}_{\mathbf{q}\nu}^s\}_{s=1,3N}$ and $\nu = 1, 3N$ indicates the phonon branches. The adiabatic/static phonon frequencies and eigenvectors are obtained considering a static perturbation, thus diagonalizing $D_{rs}(\mathbf{q}, \omega_{\mathbf{q}\nu} = 0)$.

On the other hand, the imaginary part of the force-constants matrix determines the phonon-damping

$$\gamma_{\mathbf{q}\nu} = \frac{2}{\omega_{\mathbf{q}\nu}} \sum_{s,r} \mathbf{e}_{\mathbf{q}\nu}^s A_{sr}(\mathbf{q}, \omega_{\mathbf{q}\nu}) \mathbf{e}_{\mathbf{q}\nu}^r \quad (9)$$

and the phonon linewidth.

B. Adiabatic and non-adiabatic phonons

In the previous section we have defined the non-adiabatic/dynamic phonon frequencies as the eigenvalues of the Hermitian part of the time dependent dynamical matrix, and the adiabatic/static phonon frequencies as the eigenvalues of the static time-independent dynamical matrix. Solid-state text-books^{1,16} and first-principles calculations of the phonon dispersion^{7,9,17-19}, usually treat only the adiabatic/static case, since it is commonly assumed that the adiabatic phonon frequencies coincide with the non-adiabatic ones.

In insulators, where the fundamental energy gap between the electronic ground state and the first available excited state is much larger than the phonon energy, the adiabatic/static approximation is well justified. In metals the situation is more complex.^{12,20,21}

The crucial parameter in metals is the electron relaxation time τ . In absence of electron-defect, electron-electron and electron-phonon scattering, τ is infinite. In a real metallic system, the presence of these scattering processes results in a finite relaxation time τ . We can define three cases: (i) a clean limit, when the electron relaxation time τ is much larger than the phonon period divided by 2π (ii) a dirty limit, when the electron relaxation time τ is much smaller than the phonon period divided by 2π (iii) an intermediate regime, when the electron relaxation time τ is comparable to the phonon period divided by 2π .

It has been shown^{12,20,21} that in the dirty limit the non-adiabatic phonon frequencies coincide with the adiabatic ones also in metals. Instead, in the clean limit and in the intermediate regime, the adiabatic and non-adiabatic frequencies are, in general, different.

The non-adiabatic calculations based on time-dependent DFT (described in the following sections) are performed in the perfect clean limit. Indeed, in our time-dependent calculations, the electron relaxation time τ is infinite, since we use an instantaneous (real in the frequency space) exchange-correlation Kernel, and we do not consider a broadening of the electronic levels due to defects and electron-phonon scattering.

Thus, our non-adiabatic/dynamic DFT frequencies should be used to reproduce the phonon frequencies measured in metal in the clean-limit. Instead, the adiabatic/static DFT frequencies (those generally computed with DFT linear response codes) should be used to reproduce the phonon frequencies measured in a metal in the dirty limit. Finally, to reproduce the phonon frequencies measured in a metal in the intermediate regime, one should explicitly include electron-lifetime effects in the linear response calculation, as it has been done for zone center phonon in Refs. 12,22.

By considering a single band and by linearizing the electronic-band dispersion near the Fermi energy, it has been shown²⁰ that the differences between the adiabatic and non-adiabatic phonons are largest at the center of the Brillouin zone (BZ) and vanish for $q \gg \omega_{\mathbf{q}\nu}/v_F$, where v_F is the Fermi velocity. Such differences, at the BZ center and in the clean limit, have been computed within DFT¹², and can be very sizable (up to 30% of the phonon frequency). However a detailed DFT study of non-adiabatic effect away from the BZ center (beyond a linearized one band approximation²⁰) is still missing.

C. Time dependent linear response theory

The force-constant matrix can be evaluated in the linear response theory, considering that the atomic displacement induces a perturbation in the external potential acting on the electrons.

The Hellmann-Feynmann theorem²³⁻²⁵ states that the force on atom J , $\mathbf{F}_J(t)$ can be evaluated in terms of the variation of the external potential:

$$\mathbf{F}_J(t) = - \int d\mathbf{r} n(\mathbf{r}, t) \frac{\delta V_{\text{ext}}(\mathbf{r})}{\delta \mathbf{R}_J} \quad (10)$$

where $n(\mathbf{r}, t)$ is the electronic charge density and $V_{\text{ext}}(\mathbf{r})$ is the external potential, namely:

$$V_{\text{ext}}(\mathbf{r}) = - \sum_I \frac{Z}{|\mathbf{r} - \mathbf{R}_I|} + \frac{1}{2} \sum_{I \neq J} \frac{Z_I Z_J}{|\mathbf{R}_J - \mathbf{R}_I|} \quad (11)$$

It is worthwhile to recall that $V_{\text{ext}}(\mathbf{r})$ does not depend explicitly on time but only through the dependence on time of the phonon displacement $\mathbf{u}_I(t)$. In linear response the force-constant matrix $C_{IJ}(\omega)$ is written as⁷:

$$C_{IJ}(\omega) = \int \frac{\delta n(\mathbf{r}, \omega)}{\delta \mathbf{u}_I} \frac{\delta V_{\text{ext}}(\mathbf{r})}{\delta \mathbf{u}_J} d\mathbf{r} + \int n_0(\mathbf{r}) \frac{\delta^2 V_{\text{ext}}(\mathbf{r})}{\delta \mathbf{u}_J \delta \mathbf{u}_I} d\mathbf{r}. \quad (12)$$

where $n_0(\mathbf{r})$ is the unperturbed charge density, $n(\mathbf{r}, \omega)$ is the ω -transform of the time-dependent charge density $n(\mathbf{r}, t)$ and $\frac{\delta V_{\text{ext}}(\mathbf{r})}{\delta \mathbf{u}_J}$ and $\frac{\delta^2 V_{\text{ext}}(\mathbf{r})}{\delta \mathbf{u}_I \delta \mathbf{u}_J}$ are real and time-independent quantities evaluated at the equilibrium position of the nuclei. On the contrary $\frac{\delta n(\mathbf{r}, \omega)}{\delta \mathbf{u}_I}$ is complex.

D. Time-dependent linear response in density functional theory

In this section, we examine the linear-response calculation of the real-space force-constants in the framework of density functional theory. The derivations are kept in real space as we want to keep the presence of imaginary terms (damping) in the force-constants matrix as manifest.

In order to compute $n(\mathbf{r}, \omega)$, we assume a monochromatic perturbation of the form

$$\mathbf{u}_I(t) = \mathbf{u}_I(\omega)(e^{i\omega t} + e^{-i\omega t}) \quad (13)$$

where $\mathbf{u}_I(\omega)$ is real. In density functional theory the resulting monochromatic perturbing potential is the external potential $V_{\text{ext}}(\mathbf{r})$ in Eq. 11. The derivative of the ω -transform of the charge density with respect to a ionic displacement is written as⁷

$$n_I^1(\mathbf{r}, \omega, T) = \frac{\delta n(\mathbf{r}, \omega)}{\delta \mathbf{u}_I} = 2 \sum_{\mathbf{k}i, \mathbf{k}'j}^{N_k(T)} (f_{\mathbf{k}i}(T) - f_{\mathbf{k}'j}(T)) \times \frac{\langle \psi_{\mathbf{k}'j} | \delta V_{\text{SCF}}(\mathbf{r}, \omega) / \delta \mathbf{u}_I | \psi_{\mathbf{k}i} \rangle \langle \psi_{\mathbf{k}i} | \delta V_{\text{ext}}(\mathbf{r}) / \delta \mathbf{u}_J | \psi_{\mathbf{k}'j} \rangle}{\epsilon_{\mathbf{k}i} - \epsilon_{\mathbf{k}'j} + \omega + i\eta} \psi_{\mathbf{k}i}^*(\mathbf{r}) \psi_{\mathbf{k}'j}(\mathbf{r}) \quad (14)$$

where \mathbf{k}, \mathbf{k}' label the crystal momentum, i, j are band indexes, the T is the electronic temperature (or broadening) in the Fermi function $f_{\mathbf{k}i}(T)$, η is an arbitrarily small positive real number, $N_k(T)$ is the number of \mathbf{k} -points needed to converge the sum in Eq. 14 at the electronic temperature T and the factor 2 (here and in the following) accounts for the spin-degeneracy. Finally, V_{SCF} is the Kohn-Sham self-consistent potential. The quantity $\delta V_{\text{SCF}}(\mathbf{r}, \omega) / \delta \mathbf{u}_I$ is complex and given by

$$\frac{\delta V_{\text{SCF}}(\mathbf{r}, \omega)}{\delta \mathbf{u}_I} = \frac{\delta V_{\text{ext}}(\mathbf{r})}{\delta \mathbf{u}_I} + \int K(\mathbf{r}, \mathbf{r}') n_I^1(\mathbf{r}, \omega, T) d\mathbf{r}'. \quad (15)$$

where $K(\mathbf{r}, \mathbf{r}') = \frac{\delta E_{\text{HXC}}[n]}{\delta n(\mathbf{r}) \delta n(\mathbf{r}')}$ is the kernel of the Hartree and Exchange and correlation functional, $E_{\text{HXC}}[n]$. As usual we have assumed the Hartree and exchange-correlation Kernel to be instantaneous (real in ω space).

Substitution of Eq. 14 in Eq. 12 leads to:

$$C_{IJ}(\omega, T) = 2 \sum_{\mathbf{k}i, \mathbf{k}'j}^{N_k(T)} (f_{\mathbf{k}i}(T) - f_{\mathbf{k}'j}(T)) \times \frac{\langle \psi_{\mathbf{k}'j} | \delta V_{\text{SCF}}(\mathbf{r}, \omega) / \delta \mathbf{u}_I | \psi_{\mathbf{k}i} \rangle \langle \psi_{\mathbf{k}i} | \delta V_{\text{ext}}(\mathbf{r}) / \delta \mathbf{u}_J | \psi_{\mathbf{k}'j} \rangle}{\epsilon_{\mathbf{k}i} - \epsilon_{\mathbf{k}'j} + \omega + i\eta} + \int n_0(\mathbf{r}) \frac{\delta^2 V_{\text{ext}}(\mathbf{r})}{\delta \mathbf{u}_I \delta \mathbf{u}_J} d\mathbf{r}. \quad (16)$$

where, from now on, we explicitly indicate the dependence on the electronic temperature T . This expression of the force-constants matrix is normally used in standard implementations of linear-response theory⁷.

Further substitution of Eq. 15 in Eq. 16 gives the following alternative, but equivalent formulation for the force-constants matrix in linear response theory:

$$C_{IJ}(\omega, T) = 2 \sum_{\mathbf{k}i, \mathbf{k}'j}^{N_k(T)} \frac{f_{\mathbf{k}i}(T) - f_{\mathbf{k}'j}(T)}{\epsilon_{\mathbf{k}i} - \epsilon_{\mathbf{k}'j} + \omega + i\eta} \times \langle \psi_{\mathbf{k}'j} | \frac{\delta V_{\text{SCF}}(\mathbf{r}, \omega)}{\delta \mathbf{u}_I} | \psi_{\mathbf{k}i} \rangle \langle \psi_{\mathbf{k}i} | \frac{\delta V_{\text{SCF}}(\mathbf{r}, \omega)}{\delta \mathbf{u}_J} | \psi_{\mathbf{k}'j} \rangle + \int d\mathbf{r} n_0(\mathbf{r}) \frac{\delta^2 V_{\text{ext}}(\mathbf{r})}{\delta \mathbf{u}_I \delta \mathbf{u}_J} - \int \int n_I^1(\mathbf{r}, \omega, T) K(\mathbf{r}, \mathbf{r}') n_I^1(\mathbf{r}', \omega, T) d\mathbf{r} d\mathbf{r}'. \quad (17)$$

In Eq. 17 the term including the second derivative of the external potential is real whereas all the other terms are complex. The advantage of Eq. 17 is that it allows us to introduce a variational formulation of the force-constants matrix as it will be shown in the following.

E. Variational formulation of the force-constants.

We introduce the following force-constants functional F_{IJ} :

$$F_{IJ}[\rho(\mathbf{r}), \rho'(\mathbf{r}), \omega, T] = 2 \sum_{\mathbf{k}i, \mathbf{k}'j}^{N_k(T)} \frac{f_{\mathbf{k}i}(T) - f_{\mathbf{k}'j}(T)}{\epsilon_{\mathbf{k}i} - \epsilon_{\mathbf{k}'j} - \omega + i\eta} \times \langle \psi_{\mathbf{k}'j} | \frac{\delta V_{\text{ext}}(\mathbf{r})}{\delta \mathbf{u}_I} + \int K(\mathbf{r}, \mathbf{r}') \rho(\mathbf{r}') d\mathbf{r}' | \psi_{\mathbf{k}i} \rangle \times \langle \psi_{\mathbf{k}i} | \frac{\delta V_{\text{ext}}(\mathbf{r})}{\delta \mathbf{u}_J} + \int K(\mathbf{r}, \mathbf{r}') \rho'(\mathbf{r}') d\mathbf{r}' | \psi_{\mathbf{k}'j} \rangle + \int d\mathbf{r} n_0(\mathbf{r}) \frac{\delta^2 V_{\text{ext}}(\mathbf{r})}{\delta \mathbf{u}_I \delta \mathbf{u}_J} - \int \int \rho(\mathbf{r}) K(\mathbf{r}, \mathbf{r}') \rho'(\mathbf{r}') d\mathbf{r} d\mathbf{r}'. \quad (18)$$

With this definition the force-constants matrix reads as:

$$C_{IJ}(\omega, T) = F_{IJ}[n_I^1(\mathbf{r}, \omega, T), n_J^1(\mathbf{r}, \omega, T), \omega, T] \quad (19)$$

It is straightforward to note that the force-constant functional is quadratic with respect to ρ , namely:

$$\left. \frac{\delta F_{IJ}[\rho(\mathbf{r}), \rho'(\mathbf{r}), \omega, T]}{\delta \rho(\mathbf{r})} \right|_{\rho(\mathbf{r})=n_I^1(\mathbf{r}, \omega, T), \rho'(\mathbf{r})=n_J^1(\mathbf{r}, \omega, T)} = 0. \quad (20)$$

The same relation holds upon derivation with respect to ρ' .

The consequence of Eq. 20 is that $C_{IJ}(\omega, T)$ is an extremal point and that a given error on $n_I^1(\mathbf{r}, \omega, T)$ or on $n_J^1(\mathbf{r}, \omega, T)$ affects the functional and the phonon frequencies only at second order.

Our functional formulation is related to that used for dielectric tensors by Gonze *et al.* in Ref. 26. The main difference is that, while the functional formulation of Ref. 26 is variational with respect to the first-order perturbation of the wave-function, our formulation is variational with respect to the first-order perturbation of the electronic charge density.

F. Approximated force-constants functional.

At this point we can exploit the results of the preceding section in order to develop a method to accurately calculate phonon and electron-phonon properties. Within density functional theory the most precise force-constant matrix $C_{IJ}(\omega, T)$ is obtained when T coincides with the physical temperature T_0 (*e.g.* room temperature) of the system. However, in a metal, this temperature is prohibitively small and the self-consistent calculation of $C_{IJ}(\omega, T_0)$ would be computationally unfeasible as it requires a large number of \mathbf{k} -points in order to properly converge the summation in Eq. 17. In addition, the self-consistent calculation of the imaginary part of $n_I^1(\mathbf{r}, \omega, T)$ and of $n_J^1(\mathbf{r}, \omega, T)$ at finite $\omega \neq 0$ requires to increase further the number of \mathbf{k} -points with respect to standard static linear-response calculations of $n_I^1(\mathbf{r}, 0, T)$.

A remedy to these problems is to define an approximated force constants matrix, \tilde{C}_{IJ} , as:

$$\tilde{C}_{IJ}(\omega, T_0) = F_{IJ}[n_I^1(\mathbf{r}, 0, T_{\text{ph}}), n_J^1(\mathbf{r}, 0, T_{\text{ph}}), \omega, T_0] \quad (21)$$

that is, (i) the frequency dependence on $n_I^1(\mathbf{r}, \omega, T_{\text{ph}})$ is neglected and its static limit ($\omega = 0$) is considered and (ii) n_I^1 and n_J^1 are calculated at the temperature T_{ph} instead of T_0 . The quantity T_{ph} is the electronic temperature commonly used in a self-consistent linear response calculation. Usually T_{ph} is much larger than the physical temperature T_0 , (*e.g.* $T_{\text{ph}} \approx 4000$ K)²⁷. The main consequence of the variational property of the functional F_{IJ} is that it allows us to compute phonon frequencies from an approximate force-constants matrix $\tilde{C}_{IJ}(\omega, T_0)$ in a *non self-consistent* way and performing an error that is quadratic in $|n_I^1(\mathbf{r}, \omega, T_0) - n_I^1(\mathbf{r}, 0, T_{\text{ph}})|$.

Thus, a time consuming self-consistent calculation of the non-adiabatic force-constants $C_{IJ}(\omega, T_0)$ has been replaced by an approximate non self-consistent one, $\tilde{C}_{IJ}(\omega, T_0)$, with an error that is negligible for the phonon frequencies, as it will be demonstrated in the applications considered in this work.

We now first add and subtract $C_{IJ}(0, T_{\text{ph}})$ (the standard linear-response adiabatic self-consistent force constants) in the left member of Eq. 21, and then perform

a Fourier transform to obtain:

$$\tilde{C}_{sr}(\mathbf{q}, \omega, T_0) = \Pi_{sr}(\mathbf{q}, \omega, T_0) + C_{sr}(\mathbf{q}, 0, T_{\text{ph}}) \quad (22)$$

where

$$\begin{aligned} \Pi_{sr}(\mathbf{q}, \omega, T_0) &= \\ &= \frac{2}{N_k(T_0)} \sum_{\mathbf{k}ij}^{N_k(T_0)} \frac{f_{\mathbf{k}i}(T_0) - f_{\mathbf{k}+\mathbf{q}j}(T_0)}{\epsilon_{\mathbf{k}i} - \epsilon_{\mathbf{k}+\mathbf{q}j} + \omega + i\eta} \\ &\times \mathbf{d}_{ij}^s(\mathbf{k}, \mathbf{k} + \mathbf{q}) \mathbf{d}_{ji}^r(\mathbf{k} + \mathbf{q}, \mathbf{k}) \\ &- \frac{2}{N_k(T_{\text{ph}})} \sum_{\mathbf{k}ij}^{N_k(T_{\text{ph}})} \frac{f_{\mathbf{k}i}(T_{\text{ph}}) - f_{\mathbf{k}+\mathbf{q}j}(T_{\text{ph}})}{\epsilon_{\mathbf{k}i} - \epsilon_{\mathbf{k}+\mathbf{q}j}} \\ &\times \mathbf{d}_{ij}^s(\mathbf{k}, \mathbf{k} + \mathbf{q}) \mathbf{d}_{ji}^r(\mathbf{k} + \mathbf{q}, \mathbf{k}) \end{aligned} \quad (23)$$

with the following definition of the deformation potential matrix element

$$\mathbf{d}_{mn}^s(\mathbf{k} + \mathbf{q}, \mathbf{k}) = \langle \mathbf{k} + \mathbf{q}m | \frac{\delta v_{\text{SCF}}}{\delta \mathbf{u}_{\mathbf{q}s}} | \mathbf{k}n \rangle \quad (24)$$

and where $|\mathbf{k}n\rangle$ is the periodic part of the Bloch wavefunction, *i.e.* $|\psi_{\mathbf{k}n}\rangle = e^{i\mathbf{k}\cdot\mathbf{r}}|\mathbf{k}n\rangle/\sqrt{N_k}$, and $\mathbf{u}_{\mathbf{q}s}$ is the Fourier transform of the phonon displacement \mathbf{u}_{Ls} . The integration in Eq. 24 is understood to be on the unit cell. The quantity v_{SCF} is the periodic part of the static self-consistent potential, namely $V_{\text{SCF}}(\mathbf{r}) = v_{\text{SCF}}(\mathbf{r})e^{i\mathbf{q}\cdot\mathbf{r}}$. This static self-consistent potential is calculated using standard linear response at temperature T_{ph} .

The calculation of $\Pi_{sr}(\mathbf{q}, \omega, T_0)$ requires the knowledge of band energies and eigenfunctions on a denser $N_k(T_0)$ \mathbf{k} -point grid using an electronic temperature T_0 only in an energy window of width $\sim \max(T_{\text{ph}}, \omega)$ around the Fermi level. Moreover it does not require to recalculate the derivative of the self-consistent potential. As such it is much less time consuming than a linear-response self-consistent calculation to obtain $C_{rs}(\mathbf{q}, 0, T_0)$. The non-adiabatic phonon frequencies are calculated (in the clean limit) non self-consistently from the Hermitian part of $\tilde{C}_{sr}(\mathbf{q}, \omega, T_0)$ (see Eq. 5).

The expression of the adiabatic force-constants at the physical temperature T_0 is obtained setting $\omega = 0$ in the Eq. 22:

$$\tilde{C}_{sr}(\mathbf{q}, \omega = 0, T_0) = \Pi_{sr}(\mathbf{q}, 0, T_0) + C_{sr}(\mathbf{q}, 0, T_{\text{ph}}) \quad (25)$$

In this case the force constants are Hermitian and the error in the approximated force constants is quadratic in $|n_I^1(\mathbf{r}, 0, T_0) - n_I^1(\mathbf{r}, 0, T_{\text{ph}})|$.

The advantage of the present procedure is that the linear-response self-consistent calculation is performed with a small number of \mathbf{k} -points $N_k(T_{\text{ph}})$ whereas the low temperature force constants are obtained with a non self-consistent calculation over much denser $N_k(T_0)$ \mathbf{k} -points mesh. This approach requires, as in a conventional

electron-phonon coupling calculation, the knowledge of the wavefunctions in a dense $N_k(T_0)$ k-points grid and in an energy window of the order of the maximum between T_{ph} and ω around the Fermi level, but does not require the self-consistent linear-response calculation of the derivative of the Kohn-Sham potential with respect to an atomic displacement. As such the procedure is substantially less time consuming.

G. Phonon frequencies interpolation over k-points at fixed phonon-momentum: practical implementation

The practical implementation of the above theoretical formulation for the phonon frequencies proceeds as follows:

1. Perform a standard linear response calculation *for a given phonon momentum* \mathbf{q} using a $N_k(T_{\text{ph}})$ k-points mesh and smearing T_{ph} for the electronic integration to obtain $C_{sr}(\mathbf{q}, 0, T_{\text{ph}})$.
2. In order to perform the second summation in $\Pi_{sr}(\mathbf{q}, \omega, T_0)$ (Eq. 23), calculate deformation potential matrix element of Eq. 24 on the electron-momentum grid composed of $N_k(T_{\text{ph}})$ k-points using a smearing T_{ph} .
3. Generate wavefunctions $|\mathbf{k}n\rangle$ and energies $\epsilon_{\mathbf{k}n}$ on the denser $N_k(T_0)$ electron-momentum k-points grid.
4. Perform a second non self-consistent calculation of the deformation-potential matrix-element on the more dense $N_k(T_0)$ k-points grid using smearing T_0 and v_{SCF} obtained on the $N_k(T_{\text{ph}})$ grid to obtain the first summation in $\Pi_{sr}(\mathbf{q}, \omega, T_0)$.
5. Calculate $\tilde{C}_{sr}(\mathbf{q}, \omega, T_0)$ (or $\tilde{C}_{sr}(\mathbf{q}, \omega = 0, T_0)$) using Eq. 22 (or Eq. 25).
6. Diagonalize the dynamical matrix to obtain phonon frequencies and phonon eigenvectors.

The procedure illustrated in this section is used to obtain *at a fixed phonon momentum* \mathbf{q} well converged phonon frequencies with respect to electronic k-points and smearing. Then standard Fourier interpolation can be performed to obtain dynamical matrices throughout the BZ. However, this procedure, has still two main computational shortcomings. First, the calculations of the wavefunctions and matrix elements (points 3 and 4) become cumbersome when very dense $N_k(T_0)$ k-points grid for the electron-momentum are necessary to converge. Second, in presence of phonon anomalies and not-too-smooth phonon dispersion a dense k-sampling of the phonon BZ is required.

An optimal solution to overcome these problems is represented by the use of maximally localized Wannier functions^{14,28} as an alternative electron basis function.

The method and the implementation of the Wannier functions approach for the electron-phonon interpolation is presented in Sec. III.

H. Phonon-linewidth and of the electron-phonon coupling

The imaginary part of the force-constants matrix is related to phonon-damping, namely the energy-conserving decay of a phonon in particle-hole pairs.

The imaginary part of Eq. 16 is:

$$\begin{aligned} \text{Im}(C_{IJ}(\omega, T)) &= 2 \sum_{\mathbf{k}i, \mathbf{k}'j}^{N_k(T)} (f_{\mathbf{k}i}(T) - f_{\mathbf{k}'j}(T)) \\ &\times \left(\pi \langle \psi_{\mathbf{k}'j} | \text{Re} \left[\frac{\delta V_{\text{SCF}}(\mathbf{r}, \omega)}{\delta \mathbf{u}_I} \right] | \psi_{\mathbf{k}i} \rangle \langle \psi_{\mathbf{k}i} | \frac{\delta V_{\text{ext}}(\mathbf{r})}{\delta \mathbf{u}_J} | \psi_{\mathbf{k}'j} \rangle \right. \\ &\times \delta(\epsilon_{\mathbf{k}i} - \epsilon_{\mathbf{k}'j} + \omega) \\ &+ \langle \psi_{\mathbf{k}'j} | \text{Im} \left[\frac{\delta V_{\text{SCF}}(\mathbf{r}, \omega)}{\delta \mathbf{u}_I} \right] | \psi_{\mathbf{k}i} \rangle \langle \psi_{\mathbf{k}i} | \frac{\delta V_{\text{ext}}(\mathbf{r})}{\delta \mathbf{u}_J} | \psi_{\mathbf{k}'j} \rangle \\ &\left. \times P \left[\frac{1}{\epsilon_{\mathbf{k}i} - \epsilon_{\mathbf{k}'j} + \omega} \right] \right) \end{aligned} \quad (26)$$

where P indicates the principal part. To obtain Eq. 26 we have assume that the unperturbed Hamiltonian is time-reversal symmetric so that a real set of eigenfunctions exists.

This expression is exact but it has two disadvantages. First it requires the expensive calculation of the derivative of the self-consistent potential at finite frequency both in its real and imaginary parts. Second the phonon-decay in electron-hole pairs is not manifest in the term including the principal part. These problems persist if the imaginary part of Eq. 17 is considered, since, in this functional, both $\delta V_{\text{SCF}}(\mathbf{r}, \omega)/\delta \mathbf{u}_I$ and $n_I^1(\mathbf{r}, \omega, T)$ are complex quantities. These two shortcomings are absent if the approximated force-constants matrix in Eq. 21 is used. Indeed the imaginary part of Eq. 21 is:

$$\begin{aligned} \text{Im}(\tilde{C}_{IJ}(\omega, T)) &= 2\pi \sum_{\mathbf{k}i, \mathbf{k}'j}^{N_k(T)} (f_{\mathbf{k}i}(T) - f_{\mathbf{k}'j}(T)) \\ &\times \langle \psi_{\mathbf{k}'j} | \frac{\delta V_{\text{SCF}}(\mathbf{r}, 0)}{\delta \mathbf{u}_I} | \psi_{\mathbf{k}i} \rangle \langle \psi_{\mathbf{k}i} | \frac{\delta V_{\text{SCF}}(\mathbf{r}, 0)}{\delta \mathbf{u}_J} | \psi_{\mathbf{k}'j} \rangle \\ &\times \delta(\epsilon_{\mathbf{k}i} - \epsilon_{\mathbf{k}'j} + \omega) \end{aligned} \quad (27)$$

with an error quadratic in $|n_I^1(\mathbf{r}, \omega) - n_I^1(\mathbf{r}, 0)|$. Fourier transforming and replacing Eq. 27 in Eq. 9 gives the well known equation for the phonon linewidth $\gamma_{\mathbf{q}\nu}$ full-width half-maximum (FWHM), that is:

$$\begin{aligned} \gamma_{\mathbf{q}\nu}^{\text{Fermi}} &= \frac{4\pi}{N_k(T)} \sum_{\mathbf{k}, m, n}^{N_k(T)} |g_{nm}^{\nu}(\mathbf{k}, \mathbf{k} + \mathbf{q})|^2 \\ &\times (f_{\mathbf{k}n} - f_{\mathbf{k}+\mathbf{q}m}) \delta(\epsilon_{\mathbf{k}+\mathbf{q}m} - \epsilon_{\mathbf{k}n} - \omega_{\mathbf{q}\nu}), \end{aligned} \quad (28)$$

where $g_{nm}^{\nu}(\mathbf{k}, \mathbf{k} + \mathbf{q}) = \sum_s \mathbf{e}_{\mathbf{q}\nu}^s \cdot \mathbf{d}_{mn}^s(\mathbf{k} + \mathbf{q}, \mathbf{k}) / \sqrt{2M_s \omega_{\mathbf{q}\nu}}$.

In absence of the electron-electron interaction a similar expression involving only the derivative of the bare external potential is easily obtained using Fermi golden rule. In the presence of electron-electron interaction our formalism justify the replacement of the derivative of the bare external potential by the derivative of the static screened potential $V_{\text{SCF}}(\mathbf{r}, 0)$ in the Fermi golden rule, with a well controlled error.

Under certain conditions illustrated in Refs. 29,30, the phonon linewidth can be reduced to:

$$\tilde{\gamma}_{\mathbf{q}\nu} = \frac{4\pi\omega_{\mathbf{q}\nu}}{N_k(T)} \sum_{\mathbf{k}, m, n}^{N_k(T)} |g'_{nm}(\mathbf{k}, \mathbf{k} + \mathbf{q})|^2 \times \delta(\epsilon_{\mathbf{k}n})\delta(\epsilon_{\mathbf{k}+\mathbf{q}m} - \epsilon_{\mathbf{k}n} - \omega_{\mathbf{q}\nu}) \quad (29)$$

Finally, neglecting $\omega_{\mathbf{q}\nu}$ in Eq. 29, we obtain Allen formula²⁹ namely,

$$\gamma_{\mathbf{q}\nu} = \frac{4\pi\omega_{\mathbf{q}\nu}}{N_k(T)} \sum_{\mathbf{k}, n, m}^{N_k(T)} |g'_{nm}(\mathbf{k}, \mathbf{k} + \mathbf{q})|^2 \delta(\epsilon_{\mathbf{k}n})\delta(\epsilon_{\mathbf{k}+\mathbf{q}m}) \quad (30)$$

The Allen-formula^{2,29} is widely used, and represents a good estimation of the phonon-linewidth due to electron-phonon effects, in the absence of anharmonic effects and other scattering processes. In addition, the Allen-formula relates the phonon-linewidth, as measured by inelastic Neutron or X-ray measurements, to the electron-phonon coupling as:

$$\lambda_{\mathbf{q}\nu} = \frac{\gamma_{\mathbf{q}\nu}}{2\pi\omega_{\mathbf{q}\nu}^2 \mathcal{N}_s}, \quad (31)$$

where \mathcal{N}_s is the electronic density of states per spin at the Fermi energy.

With this definition, the isotropic Eliashberg-function is

$$\alpha^2 F(\omega) = \frac{1}{2N_q} \sum_{\mathbf{q}\nu} \lambda_{\mathbf{q}\nu} \omega_{\mathbf{q}\nu} \delta(\omega - \omega_{\mathbf{q}\nu}) \quad (32)$$

where N_q is the number of phonon wavevectors. We also define the integrated electron-phonon coupling as

$$\lambda(\omega) = 2 \int_0^\omega \frac{\alpha^2 F(\omega')}{\omega'} d\omega'. \quad (33)$$

III. WANNIER FUNCTIONS

A. Wannier interpolation of the electron-phonon matrix element

In this section we explain how to interpolate the electron-phonon matrix element throughout the BZ using Wannier functions¹⁰.

Using standard first-principles methods a set of Bloch functions $\psi_{\mathbf{k}n}$ are generated with \mathbf{k} belonging to a uniform N_k^w k -points grid centered in Γ . A set of Wannier

functions centered on site \mathbf{R} are defined by the relation

$$|\mathbf{R}m\rangle = \frac{1}{\sqrt{N_k^w}} \sum_{\mathbf{k}n} e^{-i\mathbf{k}\cdot\mathbf{R}} U_{nm}(\mathbf{k}) |\psi_{\mathbf{k}n}\rangle \quad (34)$$

A suitable transformation matrix, $U_{mn}(\mathbf{k})$, must be determined in the so-called Wannierization procedure. In this work we choose to work with Maximally Localized Wannier functions (MLWF)^{14,28}, although other Wannierization schemes are possible. In the MLWF case, the matrices $U_{nm}(\mathbf{k})$ are obtained following the prescription of Refs. 14,28, which guarantees the maximal space localization of the final Wannier functions. This last requirement will be essential in the spirit of interpolation of the electron-phonon matrix elements.

Specifically, if the band-structure is formed by a composite group of bands and the number of Wannier functions is identical to the number of bands of the composite group of bands, then the matrix $U_{mn}(\mathbf{k})$ is a square matrix. On the contrary if the desired bands are entangled in a larger manifold, a preliminary disentanglement procedure from the manifold must be performed and then the square matrix $U_{mn}(\mathbf{k})$ is obtained²⁸.

The deformation potential matrix-elements $\mathbf{d}_{mn}^s(\mathbf{k} + \mathbf{q}, \mathbf{k})$ (see Eq. 24) are calculated using linear response scheme. In this calculation particular care is needed for the deformation potential at zone center, namely $\mathbf{d}_{mn}^s(\mathbf{k}, \mathbf{k})$, as explained in sec. III B.

It is crucial to note that the periodic parts $|\mathbf{k}n\rangle$ and $|\mathbf{k} + \mathbf{q}m\rangle$ entering in $\mathbf{d}_{mn}^s(\mathbf{k} + \mathbf{q}, \mathbf{k})$ have to be *exactly the same wavefunctions used for the Wannierization procedure*. If this is not the case, spurious (unphysical) phases appear in the $|\mathbf{k}n\rangle$'s (*i.e.* a phase added by the diagonalization routine or other computational reasons) and the localization properties of the Wannier functions in real space are completely lost. A way to enforce this condition is to use a uniform grid centered at Γ so that $\mathbf{k} + \mathbf{q} = \mathbf{k}' + \mathbf{G}$ with \mathbf{k}' still belonging to the original grid. In this way $|\mathbf{k} + \mathbf{q}n\rangle$ can be obtained from $|\mathbf{k}'n\rangle$ simply multiplying by a phase determined by the \mathbf{G} -vector translation and no additional phases occur.

Exploiting translational invariance, the deformation-potential matrix-element in the Wannier function basis is obtained by Fourier transform as,

$$\begin{aligned} \mathbf{d}_{mn}^s(\mathbf{R}, \mathbf{R}_L) &= \langle \mathbf{0}m | \frac{\delta V_{\text{SCF}}}{\delta \mathbf{u}_{s,L}} | \mathbf{R}n \rangle \\ &= \frac{1}{N_k^w} \sum_{\mathbf{k}, \mathbf{q}}^{N_k^w} \sum_{m', n'} e^{-i\mathbf{k}\cdot\mathbf{R} + i\mathbf{q}\cdot\mathbf{R}_L} \\ &\quad \times U_{mm'}^*(\mathbf{k} + \mathbf{q}) \mathbf{d}_{m'n'}^s(\mathbf{k} + \mathbf{q}, \mathbf{k}) U_{n'n}(\mathbf{k}) \end{aligned} \quad (35)$$

where \mathbf{R} and \mathbf{R}_L belong to a N_k^w real-space supercell. At this point it is important to underline that *the grid of N_k^w k -points on which the Wannierization process has been carried out has to be exactly the same grid for the phonon-momentum on which the dynamical matrices*

have been computed. One linear response calculation for each \mathbf{k} -point in the phonon irreducible BZ (IBZ) of the N_k^w electron \mathbf{k} -points grid has to be carried out. If this constraint is not respected, the localization properties of the electron-phonon matrix element in real space is not guaranteed.

Inverting Eq. 34, we obtain

$$|\psi_{\mathbf{k}n}\rangle = \frac{1}{\sqrt{N_k^w}} \sum_{\mathbf{R}} \sum_m e^{i\mathbf{k}\cdot\mathbf{R}} U_{nm}^*(\mathbf{k}) |\mathbf{R}m\rangle \quad (36)$$

Noting that $\mathbf{d}_{mn}^s(\mathbf{k}+\mathbf{q}, \mathbf{k}) = \frac{1}{N_k^w} \langle \psi_{\mathbf{k}+\mathbf{q}m} | \frac{\delta v_{\text{SCF}}}{\delta \mathbf{u}_{\mathbf{q}s}} | \psi_{\mathbf{k}n} \rangle$, and using Eq. 36 one obtains:

$$\mathbf{d}_{mn}^s(\mathbf{k}+\mathbf{q}, \mathbf{k}) = \frac{1}{(N_k^w)^2} \sum_L \sum_{\mathbf{R}} \sum_{m'n'} e^{i\mathbf{k}\cdot\mathbf{R}+i\mathbf{q}\cdot\mathbf{R}_L} U_{m'm}(\mathbf{k}+\mathbf{q}) \mathbf{d}_{m'n'}^s(\mathbf{R}, \mathbf{R}_L) U_{nn'}^*(\mathbf{k}) \quad (37)$$

where \mathbf{R} and \mathbf{R}_L belong to a N_k^w real-space supercell. Now, if $\mathbf{d}_{mn}^s(\mathbf{R}, \mathbf{R}_L)$ is localized inside the N_k^w real-space supercell then the interaction between different N_k^w real-space supercells can be neglected and $\mathbf{d}_{mn}^s(\mathbf{k}+\mathbf{q}, \mathbf{k})$ can be obtained from Eq. 37 via a slow Fourier transform. In practice this means that in Eq. 37 now \mathbf{k} and \mathbf{q} are any \mathbf{k} -points in the BZ. As a result of the interpolation, $\mathbf{d}_{mn}^s(\mathbf{k}+\mathbf{q}, \mathbf{k})$ can be used to calculate any physical property as in a simple tight-binding scheme.

B. Deformation potential matrix elements of optical zone-center phonons

In this section we discuss the peculiarities related to the calculation of the electron-phonon matrix elements for optical zone center phonons ($\mathbf{q} = \mathbf{0}$). The periodic part of the self-consistent potential, induced by the phonon displacement at wavelength \mathbf{q} of the atom s can be decomposed in the Coulomb (Cl) potential (the sum of the bare and Hartree potentials) and exchange-correlation (XC) contributions:

$$\frac{\delta v_{\text{SCF}}(\mathbf{r})}{\delta \mathbf{u}_{\mathbf{q}s}} = \frac{\delta v_{\text{XC}}(\mathbf{r})}{\delta \mathbf{u}_{\mathbf{q}s}} + \frac{\delta v_{\text{Cl}}(\mathbf{r})}{\delta \mathbf{u}_{\mathbf{q}s}} \quad (38)$$

The integral of the Coulomb contribution over the unit cell volume Ω is:

$$\Delta_{\mathbf{q}s} = \frac{1}{\Omega} \int d^3r \frac{\delta v_{\text{Cl}}(\mathbf{r})}{\delta \mathbf{u}_{\mathbf{q}s}}. \quad (39)$$

In DFT linear response codes, such as QUANTUM-ESPRESSO³¹, the phonon calculation with $\mathbf{q} \neq \mathbf{0}$ and $\mathbf{q} = \mathbf{0}$ are treated with two different approaches.^{7,17}

At $\mathbf{q} \neq \mathbf{0}$, the calculation is performed within the grand-canonical ensemble, with a constant electron chemical-potential (Fermi level) ϵ_F . In a metal, the limit

$$\lim_{\mathbf{q} \rightarrow \mathbf{0}} \Delta_{\mathbf{q}s} = \Delta_{0+s} \quad (40)$$

is well defined and independent on the direction of \mathbf{q} . In general one has $\Delta_{0+s} \neq 0$.

At $\mathbf{q} = \mathbf{0}$, the calculation is performed in the canonical ensemble, with a constant number of electrons. In this calculation the variation of the average Coulomb potential is conventionally set to zero, namely:

$$\Delta_{0s} = 0 \quad (41)$$

To keep constant the number of electrons the derivative of the Fermi energy with respect to the phonon displacement $\delta \epsilon_F / \delta \mathbf{u}_{\mathbf{0}s}$ can be different from zero. In particular^{7,17} it must be:

$$\frac{\delta \epsilon_F}{\delta \mathbf{u}_{\mathbf{0}s}} = -\Delta_{0+s} \quad (42)$$

In the QUANTUM-ESPRESSO implementation³¹ the $\delta v_{\text{SCF}}(\mathbf{r}) / \delta \mathbf{u}_{\mathbf{q}s}$ stored-on-disk is discontinuous at $\mathbf{q} = \mathbf{0}$, since, in this case, it does not include (as it should) the contribution from the average Coulomb potential. As a consequence the electron phonon matrix elements computed with $\delta v_{\text{SCF}}(\mathbf{r}) / \delta \mathbf{u}_{\mathbf{0}s}$ are incorrect. Moreover such discontinuity deteriorates the localization properties of the electron-phonon matrix elements in real space. The problem is easily solved by redefining the self-consistent potential to be used in the calculation of the deformation-potential matrix-elements for $\mathbf{q} = \mathbf{0}$ as:

$$\frac{\delta \tilde{v}_{\text{SCF}}(\mathbf{r})}{\delta \mathbf{u}_{\mathbf{0}s}} = \frac{\delta v_{\text{SCF}}(\mathbf{r})}{\delta \mathbf{u}_{\mathbf{0}s}} - \frac{\delta \epsilon_F}{\delta \mathbf{u}_{\mathbf{0}s}}. \quad (43)$$

Note that since $\delta \epsilon_F / \delta \mathbf{u}_{\mathbf{0}s}$ transforms under symmetry operation as a force, it is different from zero only for the atoms for which the internal coordinates are not fixed by symmetry. For this reason, $\delta \epsilon_F / \delta \mathbf{u}_{\mathbf{0}s}$ is finite in CaC_6 , while it vanishes in MgB_2 .

We remark that the same problem occurs when a frozen-phonon calculation of $\frac{\delta v_{\text{SCF}}(\mathbf{r})}{\delta \mathbf{u}_{\mathbf{0}s}}$ is carried out as in all the electronic-structure codes the average Coulomb potential is conventionally set to zero.

C. Wannier interpolation of the dynamical matrix at fixed phonon-momentum.

Steps 4, 5, 6 of section II G can be repeated using Wannier functions to interpolate at fixed phonon momentum \mathbf{q} the quantity $\Pi_{sr}(\mathbf{q}, \omega, T_0)$ to obtain Eq. 23. The advantage of the Wannier-interpolation-based strategy with respect to the procedure explained in sec. II G is that the time needed to calculate the matrix element is now negligible as there is no need to obtain, from first-principles, wavefunctions and energies on the dense $N_k(T_0)$ \mathbf{k} -point grid. Still it is necessary to perform Fourier interpolation to obtain dynamical matrices throughout the full BZ.

D. Wannier interpolation of the dynamical matrix.

In what follows we outline a strategy to obtain dynamical matrices throughout the BZ using both Fourier interpolation and Wannier functions. The method solves the main problem related to the presence of Kohn-anomalies, originating from long range interactions in the dynamical matrix. The idea is to separate in the force-constant matrix obtained in Eq. 22 in the short and long range components. The long range force constants are associated to Kohn anomalies driven by Fermi surface nesting, and, as such, they cannot be easily Fourier interpolated and require an accurate sampling of the Fermi surface. This last part will be treated using the Wannier interpolation scheme explained in section III A. On the contrary short range force constants produce smooth phonon dispersions and can be safely Fourier interpolated and do not require accurate sampling of the Fermi surface. Treating separately the two length scales permits to obtain converged phonon frequencies with respect to k-point sampling and electronic temperature, everywhere in the Brillouin zone.

This procedure is similar to the treatment of long-range dipolar forces due to the Born effective charges in polar semiconductors^{7,9}. In this case, these long range forces generate a non-analytical behavior of the dynamical matrix at zone center. While Fourier interpolation of the dynamical matrices including the non-analytical terms is impossible, it becomes possible if the long-range forces are subtracted to obtain short-range force-constants. The non-analytical part subtracted to perform Fourier interpolation is added again after Fourier interpolation.

In this spirit, we rewrite Eq. 22 as,

$$\begin{aligned} \tilde{C}_{sr}(\mathbf{q}, \omega, T_0) &= \Pi_{sr}(\mathbf{q}, \omega, T_0) \\ &- \Pi_{sr}(\mathbf{q}, 0, T_\infty) + \tilde{C}_{sr}(\mathbf{q}, 0, T_\infty) \end{aligned} \quad (44)$$

where

$$\begin{aligned} \tilde{C}_{sr}(\mathbf{q}, 0, T_\infty) &= C_{sr}(\mathbf{q}, 0, T_{ph}) + \\ &+ \Pi_{sr}(\mathbf{q}, 0, T_\infty) \end{aligned} \quad (45)$$

and T_∞ is an electronic temperature large enough in order to have only short range force constants named $\tilde{C}_{sr}(\mathbf{q}, 0, T_\infty)$, and no Kohn anomalies in the corresponding phonon branches. As a consequence, Fourier interpolation can be applied to $\tilde{C}_{sr}(\mathbf{q}, 0, T_\infty)$.

In practical implementation the procedure is the following:

1. Obtain $C_{sr}(\mathbf{q}, 0, T_{ph})$ from self-consistent linear-response phonon calculations. Such force constants are evaluated using a N_k^w k-point grid for the phonon momentum and an $N_k(T_{ph})$ k-point grid for the electron momentum.
2. Calculate $\Pi_{sr}(\mathbf{q}, 0, T_\infty)$ using the Wannier functions as described in section III C.
3. Use Eq. 45 to compute $\tilde{C}_{sr}(\mathbf{q}, 0, T_\infty)$ on the N_k^w phonon momentum grid.
4. Fourier interpolate $\tilde{C}_{sr}(\mathbf{q}, 0, T_\infty)$ to obtain dynamical matrices at any desired phonon momentum at temperature T_∞ .
5. Obtain $\tilde{C}_{sr}(\mathbf{q}, \omega, T_0)$ in Eq.44 by Wannier interpolation of $\Pi_{sr}(\mathbf{q}, \omega, T_0) - \Pi_{sr}(\mathbf{q}, 0, T_\infty)$ at any desired phonon momentum.
6. Diagonalize the dynamical matrix associated to $\tilde{C}_{sr}(\mathbf{q}, \omega, T_0, T_{ph})$ to obtain adiabatic, $\omega = 0$, or non-adiabatic (in the clean limit) $\omega = \omega_{\mathbf{q}\nu}$, phonon frequencies. These phonon frequencies include Kohn-anomalies as long range terms are properly treated by the Wannier-functions approach.

IV. APPLICATIONS

We applied the theoretical and computational framework developed in the preceding sections to two well known superconductors, namely magnesium diboride (MgB_2) and Calcium intercalated graphite (CaC_6). In these systems phonon, electron-phonon and superconducting properties are extensively investigated from both theoretical and experimental point of view and a detailed comparison can be made. At the same time, they represent non-trivial examples, where convergence problems in first-principles approaches are relevant for the calculation of phonon and superconducting properties.

A. MgB_2

Magnesium diboride (MgB_2) is, without doubts, one of the most studied and investigated materials, since 2001. The discovery of superconductivity at intermediate temperatures (40 K)³², in this compound, represented an unexpected surprise in the scientific community. Easily available, a huge amount of experimental characterizations were immediately possible³³. On the other hand, MgB_2 being composed of light elements in an hexagonal unit cell with only three atoms, allowed a first-principles computational approach for the theoretical description and understanding of its normal and superconducting properties. Density Functional Theory and linear response techniques, revealed an extraordinary high electron-phonon coupling between sp^2 bonding and anti-bonding boron orbitals, with a particular in-plane mode (E_{2g}) of the hexagonal boron sheet³⁴⁻³⁶. Based on model calculations of the electron-phonon coupling parameter ($\lambda \simeq 1$ in Ref. 35), the approximate critical temperature was estimated to be around 40 K. However, a subsequent careful investigation of the problem, revealed that the first-principles calculated values of λ , were too low to explain this high critical temperature, unless unphysical low Coulomb pseudo-potentials were

used³⁷. The solution of this inconsistency, has come with the discovery of two-band-superconductivity³⁸ in MgB₂. Two different gaps develop on the σ and π bands of the boron sheets³⁷. This allows to gain new scattering channels to enhance T_c still containing the average value of λ . At the moment, MgB₂ is classified as a two-band electron-phonon superconductor.^{39,40}

This continuous improvement of the theoretical explanation of the normal and superconducting properties of MgB₂ was in part due to some difficulties in the proper calculations of the electron-phonon coupling and of the phonon frequencies. Soon after the discovery of superconductivity in MgB₂, the first theoretical papers (based on standard DFT codes) evidenced a relevant and anomalous difficulty to properly "converge" the E_{2g} phonon frequency and the electron-phonon coupling. The reason is now clear: due to the two dimensional nature (almost cylindrical) of the σ^* Fermi surfaces electron-phonon coupling calculations require a careful integration of the Fermi surface is needed. This translates, in practical calculations, with the necessity to use an extremely dense k -space integration for electronic and phononic degree of freedom⁴¹. Although feasible in principle, it would require a huge amount of resources and computational time.

So, still after about ten years of calculations, the fundamental question about the value of the electron-phonon coupling in MgB₂, remains unanswered. This information is fundamental in order to validate the electron-phonon origin of the superconductivity in MgB₂ and at the same time, include other, still unexplored pairing interactions.

The Wannier interpolation scheme, developed in the present paper, of phonon frequencies and electron-phonon matrix elements, represents the main tool to solve this problem. It retains the first-principles character, but at the same time it is affordable from a computational point of view.

In MgB₂ the BZ-center phonon-frequency, measured by Raman spectroscopy, lies between the adiabatic and clean-limit-non-adiabatic phonon-frequency¹² computed by DFT. Thus MgB₂ is in the intermediate regime (see Sec. II B and the relaxation time estimated in Ref. 12). Since the experimental frequency at BZ center is closer to the adiabatic than the clean-limit-non-adiabatic value,¹² in MgB₂ we will not consider non-adiabatic effects, and we will present only the adiabatic dispersion.

1. Technical details

Wannier-interpolation of the MgB₂ band-structure is carried out using a $N_k^w = 6 \times 6 \times 4$ k -points grid centered at Γ using 5 Wannier functions starting from random projections. The Wannierized band structure is in excellent agreement with first-principles calculation in a 1.5 eV region from the Fermi level, as shown in Fig. 1.

The phonon dispersion and the electron-phonon ma-

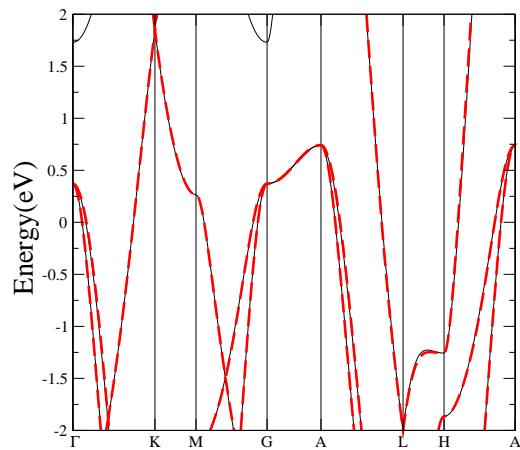


FIG. 1: (color online) Wannier-interpolated (red-dashed) and first-principles-calculated bands (black-continuous) for MgB₂. The band-energies are plotted with respect to the Fermi level.

trix element are calculated using linear-response^{7,31} on the irreducible part of the N_k^w k -points grid centered at Γ . The $\delta v_{\text{SCF}}/\delta \mathbf{u}_{\mathbf{q}s}$ on the full grid are obtained applying symmetry operations of the crystal. In the linear response calculation we perform electronic integration using a $N_k = 16 \times 16 \times 12$ k -point grid in the Brillouin zone and an Hermite-Gaussian smearing $T_{\text{ph}} = 0.025$ Ryd.

The interpolation of phonon frequencies is performed along the strategy outlined in sec. III D and using $T_\infty = 0.11$ Ryd to obtain smoothed "high temperature" phonon frequencies.

2. Adiabatic phonon dispersion

The Wannier-interpolated adiabatic phonon dispersions on different k -point grids and smearings are compared to state-of-the-art electronic structure calculations^{39,42,43} and experimental data^{5,44} in Fig. 2. In the top panel of Fig. 2 we compare the Wannier interpolated phonon dispersion with $T_0 = 0.02$ Ryd and $N_k(T_0) = 30^3$ with linear response calculations performed on selected points in the Brillouin zone using the same mesh and the same electronic temperature. The error in the interpolation scheme is always smaller than 0.5 meV. In the bottom panel of Fig. 2 we compare Wannier interpolated dispersion curves on $N_k(T_0) = 45^3$ at $T_0 = 0.01$ Ryd with Fourier interpolated linear response calculations from a $6 \times 6 \times 4$ phonon momentum grid. As can be seen anomalies are clearly found along ΓA using our new method but are completely missed by standard Fourier interpolation. The main differences with respect to previous calculations^{39,42,43} are :

1. a prominent softening (Kohn anomaly) of the two E_{2g} modes at $\mathbf{q} \approx 0.25\Gamma K$ is seen. The Kohn anomaly is also present along the ΓM high symmetry direction and in a circular region around

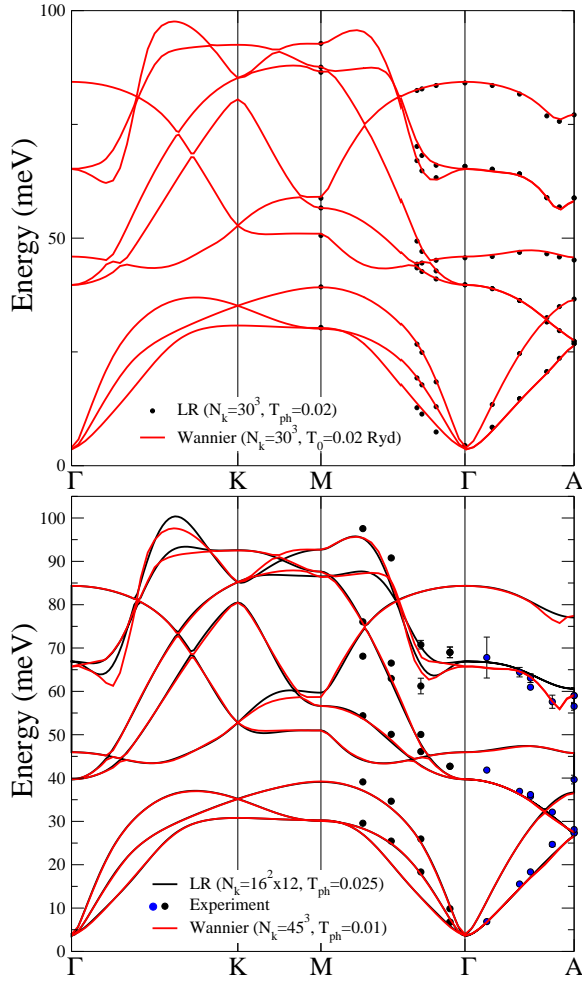


FIG. 2: (color online) Top panel: Wannier-interpolated adiabatic phonon dispersion (red line) compared to standard linear-response calculations performed on selected points in the Brillouin zone (black dots). Bottom-panel: Comparison between state-of-the-art calculated phonon dispersion using Fourier interpolation (black line) and Wannier interpolation (red line). Both interpolation schemes start from *the same* linear response calculation. Experimental data in the bottom panel are from Ref. 5 (blue circles) and from Ref. 44 (black circles). Electronic temperatures are in Rydberg. The acoustic sum rule is not applied. Interpolated branches are obtained by connecting the points at which the interpolation has been carried out in the order of increasing energy.

the zone center. Its origin is due to a in-plane nesting between the two σ cylinders. This Kohn anomaly could be probably inferred from previous calculations^{5,42,43} on smaller k-points grids although the softening of the E_{2g} modes in these works is weaker.

2. A second Kohn anomaly, absent in previous calculations^{5,42,43}, is present on the E_{2g} and B_{1g} modes along the k_z direction at $\mathbf{q} \approx 0.8\Gamma A$. This Kohn anomaly is due to nesting between different cylinders along ΓA . As it can be seen by the

comparison with previously available experimental data in Fig. 2, its presence is confirmed by inelastic X-ray scattering measurements of the phonon dispersion^{5,44}. The data at $\mathbf{q} \approx 0.8\Gamma A$ are indeed in disagreement with previous phonon dispersion calculation^{5,39,42-44} even if this disagreement was overlooked in all previous publications.

3. Overall the Wannier-interpolated phonon dispersion is in better agreement against experiments with respect to the linear-response calculated one.

These differences point out the need of having an ultra-dense k-point sampling of the Brillouin zone not only for the electron-phonon coupling but also for the phonon dispersion.

3. Electron-phonon coupling

Having interpolated the electron-phonon matrix elements and the phonon frequencies it is possible to calculate the phonon-linewidth and the electron-phonon coupling with a high degree of precision, eliminating source of errors coming from insufficient k -point sampling. In Fig. 3 the Wannier-interpolated Eliashberg-function is compared with previous calculations done with different approaches. There are two main improvements due to the better k-point sampling.

First, several previous calculations^{11,42,43} on smaller k-point grids generally overestimate the position of the main peak in $\alpha^2F(\omega)$ (centered around $\omega \approx 63$ meV in our work) due to the coupling of σ -bands with the E_{2g} phonon modes. This happens because in previous calculations the Kohn anomalies of the E_{2g} branches at $\mathbf{q} \approx 0.25\Gamma K$ was underestimated and because the anomaly along ΓA is missing. This crucial dependence of the Eliashberg function on the E_{2g} phonon frequency demonstrates the need of having both an accurate determination of λ and of the phonon frequencies to describe superconducting properties.

Second, in our work there is substantial more weight than in previous works^{11,42} in the 90-100 meV region. This energy region is dominated by the coupling of π electrons to the E_{2g} vibrations.

We now compare in more details our work with previous calculations. In the work of Bohnen *et al.*⁴³ all the peaks are up-shifted not only by the limited k-points sampling but also by the choice of using the DFT-minimized crystal structure and not the experimental one. Kong and coworkers⁴² have calculated $\lambda_{\mathbf{q}\nu}$ and $\omega_{\mathbf{q}\nu}$ on a $6 \times 6 \times 6$ phonon-momentum grid. Then for \mathbf{q} of this grid belonging to the ΓA direction the corresponding $\lambda_{\mathbf{q}\nu}$ values were replaced with some of the $12 \times 12 \times 6$ k-point grid (see Ref. 42 for more details). Fig. 3 shows that this approximation strongly overestimates the energy of the peak due to coupling between σ electronic states and the E_{2g} mode. Indeed the average electron-phonon coupling is much larger than the majority of the calcula-

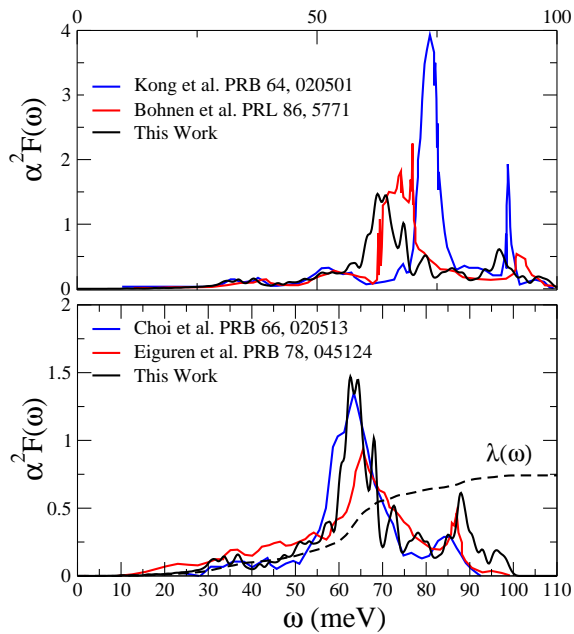


FIG. 3: (color online) Comparison of our Wannier-interpolated MgB_2 Eliashberg function with previous calculations. Kong *et al.*⁴² used first-principles calculations and a particular treatment for $\lambda_{\mathbf{q}E_{2g}}$ for \mathbf{q} along ΓA . Bohnen *et al.*⁴³ used linear response calculations while Choi *et al.*³⁹ performed frozen-phonon calculations. Finally Eiguren *et al.*¹¹ used a different implementation of Wannier interpolation on the electron-phonon matrix elements with 40^3 k-points grid for electron-momentum and 40^3 k-points grid for phonon momentum, but did not interpolate phonon frequencies. In this work we Wannier-interpolate both electron-phonon coupling (using 80^3 k-points grid for electron-momentum and 40^3 k-points grid for phonon momentum) and phonon frequencies (using 30^3 k-points grid for electron-momentum and 40^3 k-point grid for phonon momentum). The integrated $\lambda(\omega)$ from our work is also shown in the bottom panel.

tions present in literature (see Table I). Choi *et al.*³⁹ used the LDA-minimized lattice structure but surprisingly obtained *softer* E_{2g} phonon frequencies at Γ than all other works using experimental lattice parameters. In Ref. 39 the electron-phonon coupling is calculated using an interpolation scheme that does not assure the localization properties of the electron-phonon matrix element in real space. Nevertheless the position of the main peak in $\alpha^2 F(\omega)$ is similar to what we obtain. On the contrary the secondary peak related to coupling between π states and the E_{2g} mode is at too low energy. Finally, Eiguren *et al.*¹¹ used a Wannier interpolation scheme that requires an explicit calculation of the wavefunctions for any phonon momentum. The interpolation scheme was used to calculate the average electron-phonon coupling but not to interpolate phonon frequencies as they were obtained by Fourier interpolation. As a consequence

Reference	λ	ω_{\log} (meV)	N_k	N_q
Kong <i>et al.</i> [42]	0.87	62.0	$12^2 \times 6$	6^3
Bohnen <i>et al.</i> [43]	0.73	60.9	36^3	6^3
Choi <i>et al.</i> [39]	0.73	62.7	$18^2 \times 12$	$18^2 \times 12$
Eiguren <i>et al.</i> [11]	0.776		40^3	10^3
This work	0.741	58.8	80^3	20^3

TABLE I: Comparison between different electron-phonon coupling calculations in MgB_2 using different first principles methods. The label N_k (N_q) indicates the number of k-point used for electron (phonon) momentum integration.

the phonon dispersion does not present the two observed Kohn anomalies and the main peak of the $\alpha^2 F(\omega)$ is at higher energies respect to our work. This difference reflects the need of having an accurate determination of the phonon frequency in order to have converged Eliashberg functions. This appears in the lower phonon frequency logarithmic average obtained in our work with respect to previous calculations as shown in table I.

B. CaC_6

Graphite intercalated compounds represent a wide class of compounds. Due to the particular bonding properties of carbon atoms, with strong and stable sp^2 bonds and weak Van der Waals π_z bonds, graphite allows incorporation of many different atomic species between the hexagonal C sheets. Alkali metals and alkaline-earth metals are the most common, but even H, Hg, Tl, Bi, As, O, S and halogens are reported⁴⁵

The possibility to change the number of electrons in the covalent C-C bonds, always stimulated the search of superconductivity in intercalated graphite, but only in 2005 calcium intercalated graphite (CaC_6) was found to superconduct at temperatures as high as 11.5 K⁴⁶.

First-principles theoretical investigations on CaC_6 revealed that the superconducting critical temperature can be explained considering only the electron-phonon mechanism^{47,48}, even if other pairing mechanisms were proposed (excitonic and plasmonic).

The pairing originates from the electron-phonon interaction between intercalant Fermi Surface and the C out-of-plane modes and Ca in-plane modes⁴⁷. These last modes, with very low frequencies ($\simeq 15$ meV), account for about one-half of the total λ .

In this section, we re-examine the phonon and electron-phonon properties of CaC_6 , by means of the computational framework based on the Wannier interpolation.

In fact, from a computational point of view, the calculation of the energy position and \mathbf{q} -dispersion of the low energy Ca modes requires very high precision, not obtainable with the state-of-the-art phonon and electron-phonon calculations.

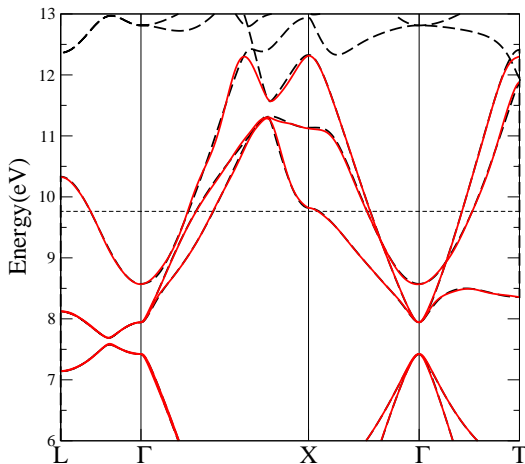


FIG. 4: (color online) Wannierized (red-dashed) and first-principles-calculated bands (black-continuous) for CaC_6 . The horizontal dashed line marks the Fermi level.

CaC_6 is well described by the clean limit regime. Indeed, the CaC_6 zone-center phonon frequency measured by Raman,^{15,49,50} is significantly larger than the DFT adiabatic one but agrees very well with the DFT clean-limit-non-adiabatic frequency^{12,15,49,50}. For this reason we will discuss both the adiabatic and the non-adiabatic dispersion.

1. Technical details

Wannier-interpolation of the CaC_6 band-structure is carried out using a $N_k^w = 6 \times 6 \times 6$ k -points grid centered at Γ . We use 7 Wannier functions starting from an initial configuration with one s -state on Calcium and one p_z state on each Carbon. The Wannierized band structure as compared to first-principles calculations is shown in Fig. 4.

We perform one linear response calculation for each point of the irreducible N_k^w k -point grid using $N_k(T_{\text{ph}}) = 8 \times 8 \times 8$ and Hermitian-Gaussian smearing $T_{\text{ph}} = 0.05$ Ryd. We then obtain $\delta v_{\text{SCF}}/\delta \mathbf{u}_{\mathbf{q}s}$ on the full grid applying the symmetry operations of the crystal. At zone center, we added a Fermi level shift to the $\mathbf{q} = 0$ component of $\delta v_{\text{SCF}}/\delta \mathbf{u}_{\mathbf{q}s}$ to obtain an analytical behavior of at $\mathbf{q} = 0$ (see section III B for more details).

The interpolation of phonon frequencies is performed along the strategy outlined in sec. III D and using $T_\infty = 0.075$ Ryd to obtain smoothed “high temperature” phonon frequencies. For the calculation of non-adiabatic phonon frequencies we chose ω in Eq. 21 as the E_{2g} phonon frequency at Γ and we also use $N_k(T_0) = 50^3$, $T_0 = 0.01$ Ryd and $\eta = 0.01$ Ryd in Eq. 23.

2. Adiabatic phonon dispersion

The phonon dispersions of CaC_6 as obtained from Fourier-interpolation and from Wannier-interpolation are illustrated in Fig. 5. The Fourier interpolate phonon dispersion is in agreement with previous linear response calculations^{47,51,52}. When compared with the more converged calculations performed using Wannier-interpolation several differences are found. The largest deviation concerns the high-energy modes at $\approx 160 - 185$ meV, in particular along ΓL . These modes involve carbon vibrations parallel to the Graphite layers (C_{xy} vibrations). There is a substantial hardening of the two highest optical phonon-modes approaching zone-boundary and a somewhat weaker softening close to zone center. The shape of the phonon dispersion of the two highest optical modes along ΓL recalls the typical behavior of the real-part of the phonon self-energy due to electron-phonon coupling (see for example for the case of MgB_2 Ref. 30, fig 3a.). The electron-phonon coupling to these optical modes comes essentially from π^* states and mostly from intraband-coupling⁵³ (small Fermi surface) so that a quite accurate BZ sampling is necessary to display this behavior. This explains the strong k -point dependence of the result.

Moreover the relevance of having an accurate sampling of the Fermi surface is evident from the large number of Kohn-anomalies (arrows in Fig. 5 mark the occurrence of a Kohn-anomaly) present in the Wannier-interpolated branches and almost always absent in the Fourier interpolated ones. At high energy (150-180 meV) we count a large number of anomalies, no one of which is present in Fourier interpolated branches. These anomalies are mostly located close to the X and χ points. At low energy we count 8 more softenings, 6 of which involve points close to the X-point (although on different branches) and two occur at the χ point. In Fourier interpolated calculations only a very broad anomaly is visible in the low energy modes, located exactly at the X-point, nothing in other energy modes. The facts that close to the X point (i) several anomalies at the same vector occur on different modes and that (ii) the phonon frequencies associated to the anomaly are strongly dependent on the electronic temperature suggest an origin dependent from the Fermi surface geometry. Indeed this is the case and the anomaly is illustrated in the nesting vector in Fig. 6.

3. Non-adiabatic phonon dispersion

Non-adiabatic effects occur in CaC_6 close to zone center^{12,15}. However it is unknown how strong are these effects far from zone center, namely what is the degree of localization of non-adiabatic effects around the Γ point. The question is meaningful as if non-adiabatic effects extend substantially in the Brillouin zone then they can be relevant for superconductivity and transport as the average electron-phonon coupling and the critical tem-

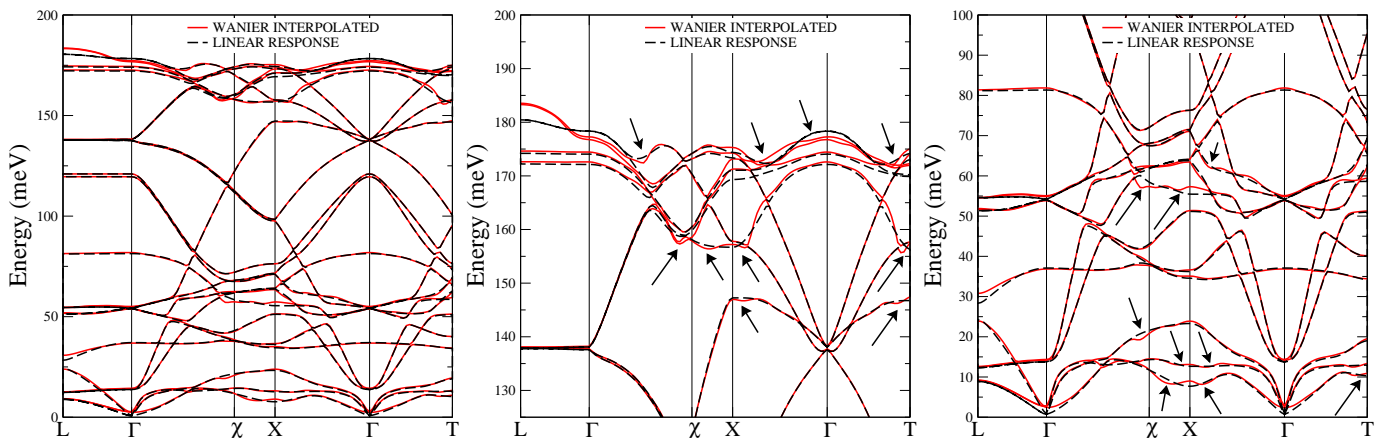


FIG. 5: (color online) Wannier-interpolated (red-continuous) and Fourier-interpolated (black-dashed) adiabatic phonon dispersion in CaC_6 . The center and right panels are zooms to the high and low energy parts of the phonon dispersion. The Fourier-interpolated phonon branches are obtained from the dynamical matrices calculated on a $N_k^w = 6^3$ phonon grid, using $N_k = 8^3$ and Hermite-Gaussian smearing $T_{\text{ph}} = 0.05$ Ryd. The Wannier interpolated bands are obtained on a $N_k = 40^3$ and Hermitian-Gaussian smearing $T_{\text{ph}} = 0.01$ Ryd. The Kohn-anomalies are indicated by arrows.

Reference	λ	ω_{\log} (meV)	N_k	N_q
Calandra <i>et al.</i> [47]	0.83	24.7	$6 \times 6 \times 6$	$4 \times 4 \times 4$
Kim <i>et al.</i> [52]	0.84	26.28	$8 \times 8 \times 8$	$4 \times 4 \times 4$
Sanna <i>et al.</i> [48]	0.85	28.0	$6 \times 6 \times 6$	$6 \times 6 \times 6$
This work	0.829	27.9	59^3	20^3

TABLE II: Comparison between different electron-phonon coupling calculations for CaC_6 using different first principles methods. The label N_k (N_q) indicates the number of k-point used for electron (phonon) momentum integration.

perature could be affected.

In Fig. 7 we plot the Wannier-interpolated non-adiabatic phonon dispersion. At Γ we obtain $\omega^{NA} = 190$ meV (≈ 1532 cm^{-1}), in good agreement with what found in Ref. 12. Most interestingly the full E_{2g} branch is shifted to higher energies (particularly along ΓL , the k_z direction) by the non-adiabatic effects. Even at half-way to the zone border the correction is sizable and it can be easily measured with inelastic X-ray or Neutron scattering experiments. In the case of CaC_6 as the high-energy modes are weakly-coupled to electrons the non-adiabatic correction, even if large, probably does not affect the critical temperature. The situation can be substantially different in other superconductors so that non-adiabatic effects have to be taken into account to describe the electron-phonon interaction in layered superconductors.

4. Electron-phonon coupling

The Eliashberg function calculated with the adiabatic phonon frequencies and the integrated electron-phonon coupling for CaC_6 are illustrated in Fig. 8. The situation

is very similar to previous works in what concern the average value of the electron-phonon coupling, as shown in table II.

Previous calculations performed using standard linear-response methods report similar values of λ and a 13% variation is present on ω_{\log} (see table II). Our calculation confirms the largest value reported in literature.

V. CONCLUSIONS

In this work we developed a first-principles variational scheme to calculate adiabatic and non-adiabatic phonon frequencies in the full Brillouin zone. We demonstrated how the method permits the calculation of phonon dispersion curves free from convergence issues related to Brillouin zone sampling. Our approach also justify the use of the static screened potential in the calculation of the phonon linewidth due to decay in electron-hole pairs.

We apply the method to the calculation of the phonon dispersion and electron-phonon coupling in MgB_2 and CaC_6 . In both compounds we demonstrate the occurrence of several Kohn anomalies, absent in previous works, that are manifest only after careful electron and phonon momentum integration. In MgB_2 , the presence of Kohn anomalies on the E_{2g} branches improves the agreement with measured phonon spectra and affects the position of the main peak in the Eliashberg function. In CaC_6 we show that the non-adiabatic effects on in-plane carbon vibrations are not localized at zone center but are sizable throughout the full Brillouin zone. Thus NA effects can be relevant for the determination of the superconducting properties of layered superconductors. In general our work underlines the important of obtaining accurate (well converged) phonon frequencies to determine the electron-phonon coupling and superconducting

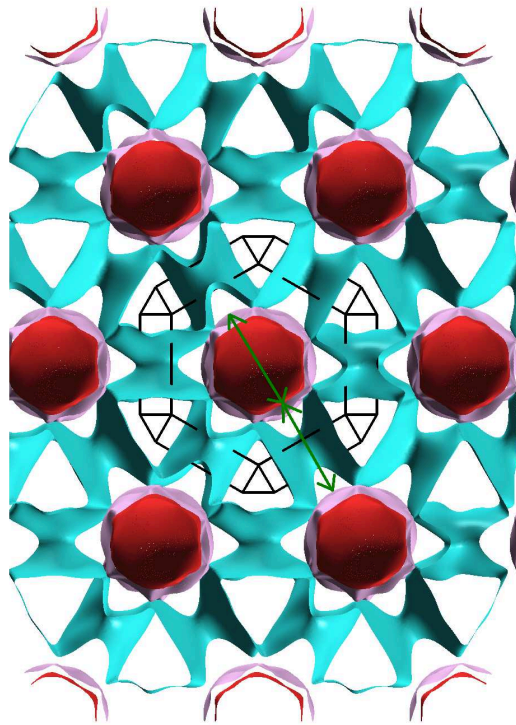


FIG. 6: (Color online) Fermi surface of CaC_6 calculated using Wannier-functions on a 100^3 k-points grid. The green arrows mark the nesting vectors responsible for the Kohn-anomaly close to X.

properties in a reliable way.

The large gain in the computational time necessary to obtain phonon dispersion provided by our theoretical scheme opens new perspectives in large-scale first-principles calculations of dynamical properties and electron-phonon interaction. Furthermore, the variational property of the force constants functional with respect to the first-order perturbation of the electronic charge density is a property that can be generalized to the calculation of other response functions such as optical properties and the calculation of Knight shifts as measured in nuclear magnetic resonance⁵⁴.

VI. ACKNOWLEDGEMENTS

We acknowledge fruitful discussion with J. Yates and support from ANR PNANO-ACCATTONE. GP acknowledges support from CNRS. Calculations were performed at the IDRIS supercomputing center and at Cineca (Bologna, Italy) through an INFN-CNR supercomputing.

¹ J. M. Ziman, *Electron and Phonons* (Clarendon Press, Oxford, 2001).

² G. Grimvall, *The electron-phonon interaction in metals*, (North Holland, Amsterdam, 1981)

³ J. R. Schrieffer, *Theory of Superconductivity* (Addison Wesley, 1988).

⁴ R. E. Peierls, *Quantum theory of solids* (Oxford University Press, 2001)

⁵ Abhay Shukla, Matteo Calandra, Matteo d'Astuto, Michele Lazzeri, Francesco Mauri, Christophe Bellin, Michael Krisch, J. Karpinski, S. M. Kazakov, J. Jun, D. Daghero, and K. Parlinski, *Phys. Rev. Lett.* **90**, 095506 (2003)

⁶ M. Born and J. R. Oppenheimer, *Ann. Physik* **84**, 457 (1927)

⁷ S. Baroni, S. de Gironcoli, A. Dal Corso, and P. Giannozzi,

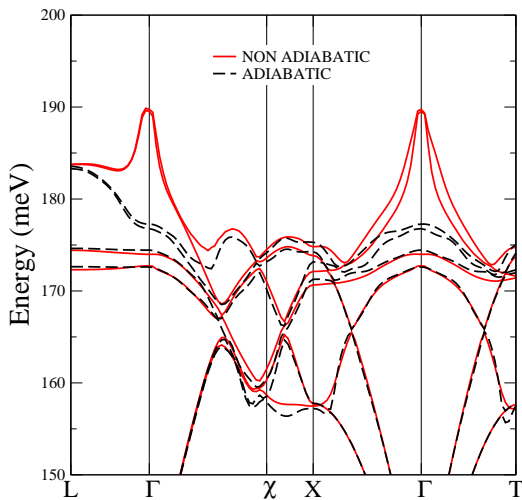


FIG. 7: (color online) Wannier-interpolated non-adiabatic (red-continuous) and adiabatic (black-dashed) phonon dispersion in CaC_6 .

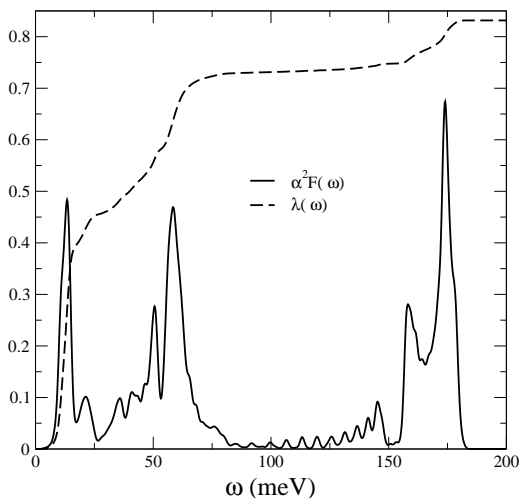


FIG. 8: (color online) Wannier-interpolated Eliashberg function and integrated Eliashberg functions for CaC_6 . Note that the wiggles in the 80-150 meV region are not due to poor convergence but to the presence of many well separated dispersive branches in this energy region.

Rev. Mod. Phys. **73**, 515 (2001)

- ⁸ S. Y. Savrasov and D. Y. Savrasov, Phys. Rev. B **54**, 16487 (1996)
- ⁹ X. Gonze, C. Lee, Phys. Rev. B **55**, 10355 (1997)
- ¹⁰ F. Giustino, M. L. Cohen, and S. G. Louie, Phys. Rev. B **76**, 165108 (2007)
- ¹¹ A. Eiguren and C. Ambrosch-Draxl, Phys. Rev. B **78**, 045124 (2008).
- ¹² A. M. Saitta, M. Lazzeri, M. Calandra, and F. Mauri, Phys. Rev. Lett. **100**, 226401 (2008)
- ¹³ F. Giustino, J. R. Yates, I. Souza, M. L. Cohen, and S. G. Louie, Phys. Rev. Lett. **98**, 047005 (2007)
- ¹⁴ N. Marzari and D. Vanderbilt, Phys. Rev. B **56**, 12847-12865 (1997)

- ¹⁵ M. P. M. Dean, C. A. Howard, S. S. Saxena, and M. Ellerby, Phys. Rev. B **81**, 045405 (2010)
- ¹⁶ see e.g. N. W. Ashcroft and N. D. Mermin, Solid State Physics (Holt, Rhinehard and Winston, New York, 1976), Chap. 26, page 529, footnote 31.
- ¹⁷ de Gironcoli, S., 1995, Phys. Rev. B **51**, 6773.
- ¹⁸ A. A. Quong and B. M. Klein, Phys. Rev. B **46**, 10734 (1992)
- ¹⁹ S. Y. Savrasov, Phys. Rev. Lett. **69**, 2819 (1992)
- ²⁰ E. Maksimov and S. V. Shulga, Solid State Communication **97**, 553 (1996)
- ²¹ M. Calandra, M. Lazzeri and F. Mauri, Physica C **456**, 38 (2007)
- ²² E. Cappelluti, Phys. Rev. B **73**, 140505 (2006).
- ²³ Hellmann, H., 1937, *Einführung in die Quantenchemie* (Deuticke, Leipzig).
- ²⁴ Feynman, R. P., 1939, Phys. Rev. **56**, 340.
- ²⁵ M. Di Ventra and S. T. Pantelides, Phys. Rev. B **61**, 16207 (2000)
- ²⁶ X. Gonze, D. C. Allan and M. P. Teter, Phys. Rev. Lett. **68**, 3603 (1992).
- ²⁷ In principle, the force constants matrix depends implicitly on the temperature used in the self-consistent calculation of $n_0(\mathbf{r})$, $\epsilon_{\mathbf{k},i}$ and $\psi_{\mathbf{k},i}(\mathbf{r})$. Moreover, the dependence of force constants on this last temperature is weak and thus it is usually taken (as in the present derivation) equal to T_{ph} . However, it should be set equal to the physical temperature, T_0 as a single standard self-consistent calculation does not poses relevant problems in k-point convergence.
- ²⁸ N. Marzari and D. Vanderbilt, Phys. Rev. B **65**, 035109 (2001)
- ²⁹ P. B. Allen, Phys. Rev. B **6**, 2577 (1972), P. B. Allen and R. Silbergliitt, Phys. Rev. B **9**, 4733 (1974).
- ³⁰ Matteo Calandra and Francesco Mauri, Phys. Rev. B **71**, 064501 (2005)
- ³¹ P. Giannozzi et al. J. Phys.: Condens. Matter **21**, 395502 (2009)
- ³² J. Nagamatsu, N. Nakagawa, T. Muranaka, Y. Zenitani, and J. Akimitsu, Nature **410**, 63 (2001).
- ³³ Recent Advances in MgB2 Research, Physica C **456** (2007).
- ³⁴ J. Kortus, I. I. Mazin, K. D. Belashchenko, V. P. Antropov, and L. L. Boyer, Phys. Rev. Lett. **86**, 4656 (2001).
- ³⁵ J. M. An and W. E. Pickett, Phys. Rev. Lett. **86**, 4366 (2001).
- ³⁶ Y. Kong, O.V. Dolgov, O. Jepsen, and O.K. Andersen, Phys. Rev. B **64**, 020501 (2001).
- ³⁷ A. Y. Liu, I. I. Mazin, and J. Kortus, Phys. Rev. Lett. **87**, 087005 (2001).
- ³⁸ F. Giubileo et al., Phys. Rev. Lett. **87**, 177008 (2001).
- ³⁹ H. J. Choi et al., D. Roundy, H. S., M. L. Cohen, and S. G. Louie, Nature (London) **418**, 758 (2002), H. J. Choi, D. Roundy, H. S., M. L. Cohen, and S. G. Louie, Phys. Rev. B **66**, 020513 (2002).
- ⁴⁰ A. Floris et al., Phys. Rev. Lett. **94**, 037004 (2005).
- ⁴¹ M. Calandra and F. Mauri, Phys. Rev. B **71**, 064501 (2005).
- ⁴² Y. Kong, O. V. Dolgov, O. Jepsen, and O. K. Andersen, Phys. Rev. B, **64**, 020501(R) (2001).
- ⁴³ K. P. Bohnen, R. Heid and B. Renker, Phys. Rev. Lett. **86** 5771 (2001).
- ⁴⁴ Matteo d'Astuto, Matteo Calandra, Stephanie Reich, Abhay Shukla, Michele Lazzeri, Francesco Mauri, Janusz Karpinski, N. D. Zhigadlo, Alexei Bossak, and Michael

- Krisch, Phys. Rev. B **75**, 174508 (2007) .
- ⁴⁵ N. Emery *et al.*, Sci. Technol. Adv. Mater. **9** 044102 (2008).
- ⁴⁶ T. E. Weller, M. Ellerby, S. S. Saxena, R. P. Smith and N. T. Skipper, Nat. Phys. **1**, 39 (2005).
- ⁴⁷ M. Calandra and F. Mauri, Phys. Rev. Lett. **95**, 237002 (2005)
- ⁴⁸ A. Sanna, G. Profeta, A. Floris, A. Marini, E. K. U. Gross and S. Massidda, Phys. Rev. B **75**, 020511 (2007)
- ⁴⁹ J. Hlinka, I. Gregora, J. Pokorny, C. Hérold, N. Emery, J. F. Marêché, and P. Lagrange Phys. Rev. B **76**, 144512 (2007)
- ⁵⁰ A. Mialitsin, J. S. Kim, R. K. Kremer, and G. Blumberg Phys. Rev. B **79**, 064503 (2009)
- ⁵¹ Matteo Calandra and Francesco Mauri, Phys. Rev. B **74**, 094507 (2006)
- ⁵² J. S. Kim, L. Boeri, R. K. Kremer, and F. S. Razavi Phys. Rev. B **74**, 214513 (2006)
- ⁵³ L. Boeri, G. B. Bachelet, M. Giantomassi, and O. K. Andersen, Phys. Rev. B **76**, 064510 (2007).
- ⁵⁴ M. d’Avezac, N. Marzari and F. Mauri, Phys. Rev. B **76**, 165122 (2007)